UKAEA-CCFE-PR(23)81

M. Giacomin, D. Dickinson, D. Kennedy, B. Patel, C. M. Roach

Numerical investigation of microtearing modes in the tokamak core of experimentally relevant spherical tokamak scenarios

Numerical investigation of microtearing modes in the tokamak core of experimentally relevant spherical tokamak scenarios

M. Giacomin, D. Dickinson, D. Kennedy, B. Patel, C. M. Roach

This is a preprint of a paper submitted for publication in
To be decided

Numerical investigation of microtearing modes in the core of experimentally relevant spherical tokamak scenarios

M. Giacomin[1], D. Dickinson[1], D. Kennedy[2], B. Patel[2] and C. M. Roach[2]

[1]York Plasma Institute, University of York, York, YO10 5DD, United Kingdom
[2]Culham Centre for Fusion Energy, Abingdon OX14 3DB, United Kingdom

E-mail: `maurizio.giacomin@york.ac.uk`

Abstract. Linear and nonlinear gyrokinetic simulations are performed in experimentally relevant scenarios built from a MAST case where a microtearing mode instability dominates at ion Larmor radius scale. While this equilibrium is taken from MAST, microtearing modes are only weakly unstable on the surface analysed here and are not believed to dominate the experimental transport. This collisional microtearing mode instability appears only when a velocity dependent electron collision frequency is considered. Electrostatic potential fluctuations are found to provide a strong destabilisation mechanism. The sensitivity to the electron collision frequency is investigated in both linear and nonlinear simulations. While the effect of electron collision frequency is moderate in linear simulations, a strong dependence on this parameter is found in nonlinear simulations. The effect of magnetic islands generated by microtearing modes and their interaction is analysed, showing that the radial extension of the stochastic region caused by islands overlapping plays an important role in determining the saturation level of the microtearing mode driven heat flux and it is consistent with the heat flux increase observed in nonlinear simulations at low electron collision frequency values. The magnetic shear is found to play an important role in the formation of a stochastic layer.

1. Introduction

Previous theoretical and numerical works have shown the presence of a linear tearing instability at high mode numbers driven by an electron temperature gradient and denoted as microtearing mode (MTM) [1]. Recent nonlinear simulations have shown that the MTM instability can significantly contribute to the electron heat flux in the edge of H-mode plasmas as well as in the core of spherical tokamaks (see, e.g., Refs. [2–6]). The first theoretical description of the MTM instability has been proposed in Ref. [1] and extended later in Refs. [7–12]. In particular, Ref. [7] shows that the MTM instability separates into three regimes depending on the electron collision frequency, $\nu_e = 4\pi n_e e^4 \ln\lambda/[(2T_e)^{3/2} m_e^{1/2}]$ (n_e is the electron density, λ is the Coulomb logarithm, T_e is the electron temperature and m_e is the electron mass): a collisionless regime with $\nu_e \ll \omega$, a semi-collisional regime with $\nu_e \ll (k_\parallel v_{\mathrm{th,e}})^2/\omega$ and $\nu_e > \omega$ (with $v_{\mathrm{th,e}} = \sqrt{2T_e/m_e}$ the electron thermal velocity and $k_\parallel$ the parallel wave vector), and a collisional regime with $\nu_e \gg \omega$, where ω is the MTM frequency. The work in Ref. [7] neglects the effect of the electrostatic potential in the collisionless and semi-collisional regimes. A following numerical analysis has extended this work by including the effect of electrostatic potential fluctuations, showing that these provide a strong destabilising effect [8], also confirmed in recent linear gyrokinetic simulations [13]. While first linear studies show that the mechanism driving the collisional MTM instability requires a velocity dependent collision frequency [9], unstable (collisional) MTMs have been found also when a velocity independent collision operator is considered [14], highlighting the presence of various driving mechanisms.

A magnetic perturbation δB_{mn} associated with MTMs resonates at the rational surface with $q = m/n$, where q is the safety factor, m and n are the poloidal and toroidal magnetic perturbation mode number, respectively. Resonant modes can reconnect and form magnetic islands. An estimate of the island width is derived in Ref. [15],

$$w_{\mathrm{island}} = 4\sqrt{\frac{\delta B}{B_0}\frac{rR}{ns}}\,, \tag{1}$$

where B_0 is the unperturbed magnetic field, r the tokamak minor radius, R the tokamak major radius and $s = (r/q)\mathrm{d}q/\mathrm{d}r$ is the magnetic shear. The distance between two rational surfaces with consecutive m and same n, corresponding to $q(r_m) = m/n$ and $q(r_{m+1}) = (m+1)/n$, is approximated by

$$\Delta r \simeq 1/(nq') = r/(nqs)\,, \tag{2}$$

where $q' = \mathrm{d}q/\mathrm{d}r$. When more toroidal modes are considered, the minimum distance between two adjacent rational surfaces with $q(r_{mn}) = m/n$ and $q(r_{m'n'}) = m'/n'$ can be approximated by [16, 17]

$$\delta r \simeq \frac{r\Delta n}{n^2 qs}\,, \tag{3}$$

where $\Delta n = n' - n$ is the separation between toroidal mode numbers. If the magnetic island width is larger than the distance between two adjacent rational surfaces, a region of stochastic magnetic field lines can form [17]. Magnetic field stochasticity can provide a strong transport mechanism, as described in Ref. [18], thus accounting for the significant electron heat flux observed in nonlinear gyrokinetic MTM simulations [2]. In addition, electron heat transport consistent with the island overlap criterion has been observed in NSTX experiments [16].

While linear gyrokinetic simulations have been extensively carried out and show the presence of MTMs in many experimentally relevant scenarios [4, 14, 19–24], an accurate estimate of the electron heat flux driven by MTMs requires one to perform nonlinear gyrokinetic simulations, which remain very challenging because of the high numerical requirements [3]. In recent years, significant effort has been devoted to understand the mechanisms behind the saturation of the MTM driven electron heat flux. For example, Ref. [2] shows that the MTM driven heat flux can be significantly reduced by equilibrium flow shear. Zonal fields [6] and local temperature flattening [25] have also been found to saturate MTM turbulence. In Ref. [5], ion-scale MTMs are suppressed by electron-scale turbulence via cross-scale nonlinear interactions.

Here, we analyse the result of linear and nonlinear gyrokinetic simulations of experimentally relevant cases built from the MAST discharge #22769. These cases are characterised by a dominant ion scale collisional MTM instability, whose dependence on various parameters and, in particular, on the electron collision frequency is investigated. While the electromagnetic heat flux from MTMs is very low and not experimentally significant on the chosen surface in this discharge, the local equilibrium nevertheless provides a useful reference for a scientific study of nonlinear saturation of MTMs in numerically tractable conditions close to marginal stability. Saturation mechanisms are investigated, and indicate a significant contribution from zonal fields in the saturation process, thus supporting Ref. [6]. In addition, the level of saturated heat flux is found to strongly depend on the radial extension of the stochastic region due to magnetic island overlapping.

This paper is organised as follows. The MAST reference case is introduced in Sec. 2, where the dominant microinstabilities are identified by means of linear gyrokinetic simulations. In Sec. 3, the main MTM instability is characterised and results from linear simulation scans in electron temperature gradient, density gradient and electron collision frequency are presented. Results of nonlinear simulations are reported in Sec. 4, where the main saturation mechanism is identified. Finally, the effect of the stochastic layer formation on heat flux is analysed in Sec. 5. Conclusions follow in Sec. 6.

2. The MAST reference case

The reference case is based on the MAST discharge #22769, which corresponds to the high collisionality discharge of Ref. [21]. The equilibrium magnetic flux surfaces for this discharge are shown in Fig. 1 at $t = 0.2$ s. The linear gyrokinetic analysis of Ref. [21] points out the presence of a MTM instability at ion Larmor radius scales, thus suggesting a possible important role played by MTMs in this discharge. This case is therefore considered as a baseline scenario to characterise and analyse MTM turbulence and transport. Details on the equilibrium and profiles are reported in Ref. [21].

In this work, we perform local linear and nonlinear gyrokinetic simulations at a radial surface located in the middle of the tokamak core ($r/a = 0.5$) and depicted as a red line in Fig. 1. The safety factor and magnetic shear profiles in a region around $r/a = 0.5$ are also shown in Fig. 1. A Miller parameterisation [26], obtained by fitting this radial surface using the `pyrokinetics` python library [27], is considered in the following. Local parameters are reported in table 1.

Fig. 2 shows the growth rate and mode frequency of the dominant mode as a function of k_y from linear simulations carried out by using the gyrokinetic code GS2 [28,29], with k_y the binormal wave vector, $\rho_s = c_s/\Omega_i$ the ion sound Larmor radius, $c_s = \sqrt{T_e/m_D}$ the ion sound speed, $\Omega_i = eB/m_D$ the ion cyclotron frequency and m_D

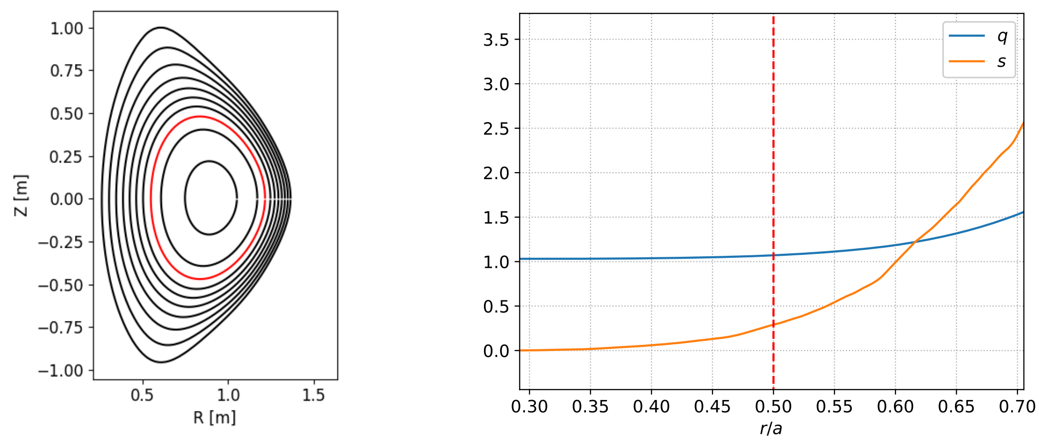

(a) **(b)**

Figure 1: *(a) Contour plot of the equilibrium poloidal magnetic flux for the MAST discharge #22769 at* $t = 0.2$ *s [21]. The red line corresponds to the radial surface where the gyrokinetic linear and nonlinear simulations are performed. (b) Safety factor and magnetic shear profile in the region* $r/a \in [0.3, 0.7]$ *around the relevant radial surface at* $r/a = 0.5$*. The red dashed vertical line indicates the radial position of the reference surface.*

MAST #22769 at r/a = 0.5	
q	1.07
$\hat{s}$	0.34
ρ_*	0.015
κ	1.41
δ	0.23
Δ'	-0.13
β_e	0.057
ν_*	0.1
n_e	3.6×10^{19} m^{-3}
T_e	450 eV
a/L_n	0.22
a/L_{T_e}	2.1
a/L_{T_D}	1.7

Table 1: *Local parameters of the MAST discharge #22769 [21] at mid radius. The parameters* δ, κ, Δ', ν_*, a/L_n *and* a/L_T *denote the plasma triangularity, the elongation, the Shafranov shift, the collisionality, and the normalised inverse gradient lengths for density and temperature, respectively, with* $\rho_* = \rho_s/a$, $\nu_* = \nu_e q R/(\epsilon^{3/2} v_{\mathrm{th,e}}) \simeq 0.1$, $\epsilon = r/R$ *and* a *the tokamak minor radius.*

	GS2		CGYRO
	ETG	MTM	MTM
n_θ	32	64	64
n_r	17	65	64
n_λ, n_ξ	24	24	24
n_ϵ	8	8	8

Table 2: *Numerical resolution used in GS2 and CGYRO linear simulations, with n_θ and n_r the number of grid points in the parallel and radial directions, respectively, and n_ϵ the number of the energy grid points. In GS2 n_λ is the number of pitch-angles, while n_ξ is the number of Legendre pseudospectral meshpoints in the pitch-angle space in CGYRO. A higher radial resolution in CGYRO, $n_r = 128$, is required in some cases to achieve an accurate agreement between CGYRO and GS2 linear results. Results of CGYRO linear simulations are presented in Sec. 3.*

the deuterium mass. We note in Fig. 2 the presence of two different instabilities at ion and electron Larmor radius scale. The mode frequency of both instabilities is in the electron diamagnetic direction (negative sign is used here for frequency in the electron diamagnetic direction). The maximum growth rate of the electron scale instability is two orders of magnitude larger than the one of the ion scale instability. The numerical resolution used in GS2 linear simulations is reported in table 2. Results of convergence tests are shown in Appendix A.

The real and imaginary components of the electrostatic potential $\delta\phi$ and $\delta A_\parallel$ are shown in Fig. 3 as a function of the ballooning angle θ at the two different values of k_y corresponding to the maximum growth rate of the ion and electron scale instabilities. The ion scale instability is characterised by $\delta\phi$ extended along θ, while $\delta A_\parallel$ is very narrow around $\theta = 0$. The mode has a tearing parity, i.e. $\delta\phi$ has odd parity and $\delta A_\parallel$ even parity with respect to $\theta = 0$. These are common features of a MTM instability [14]. The mode at electron scale has a twisting parity ($\delta\phi$ even and $\delta A_\parallel$ odd), with both $\delta\phi$ and $\delta A_\parallel$ localised in the region of $\theta = 0$. Electron scale modes are driven unstable by an electron temperature gradient (ETG) instability. This agrees with previous gyrokinetic linear simulations that have pointed out the presence of the ETG instability in various MAST scenarios [30]. We note that the amplitudes of $\delta\phi$ and $\delta A_\parallel$, normalised to $\max|\delta\phi$, are comparable at $k_y\rho_s = 0.5$, while $\delta\phi \gg \delta A_\parallel$ at $k_y\rho_s = 20$. This is consistent with the ion (electron) scale instability being electromagnetic (electrostatic).

In this work, we focus only on the MTM instability, although the ETG instability drives most of the turbulent transport at the chosen radial surface of this MAST scenario, as shown in Appendix B. In fact, we highlight that the aim of the present paper is to investigate the saturation mechanism of this MTM instability and the role of the stochastic layer rather than to provide an accurate prediction of the heat flux in this MAST case.

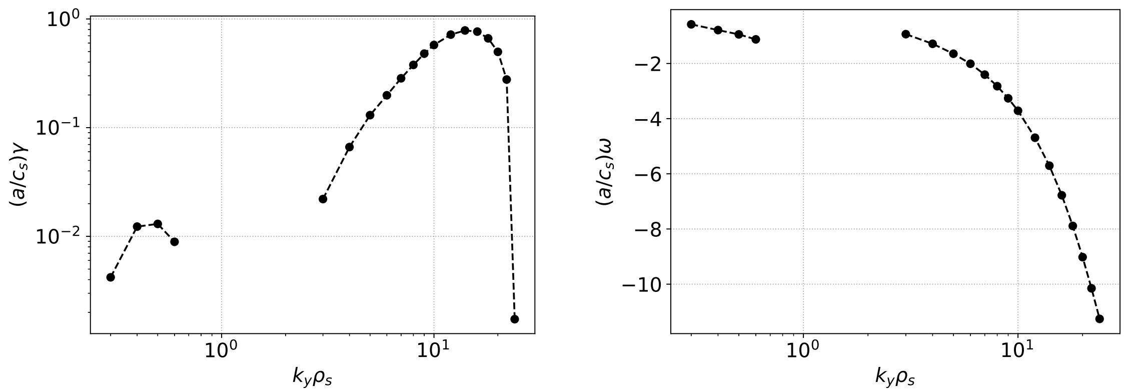

(a) **(b)**

Figure 2: *Growth rate (a) and mode frequency (b) as a function of k_y. Only unstable modes are shown. Results from linear GS2 simulations.*

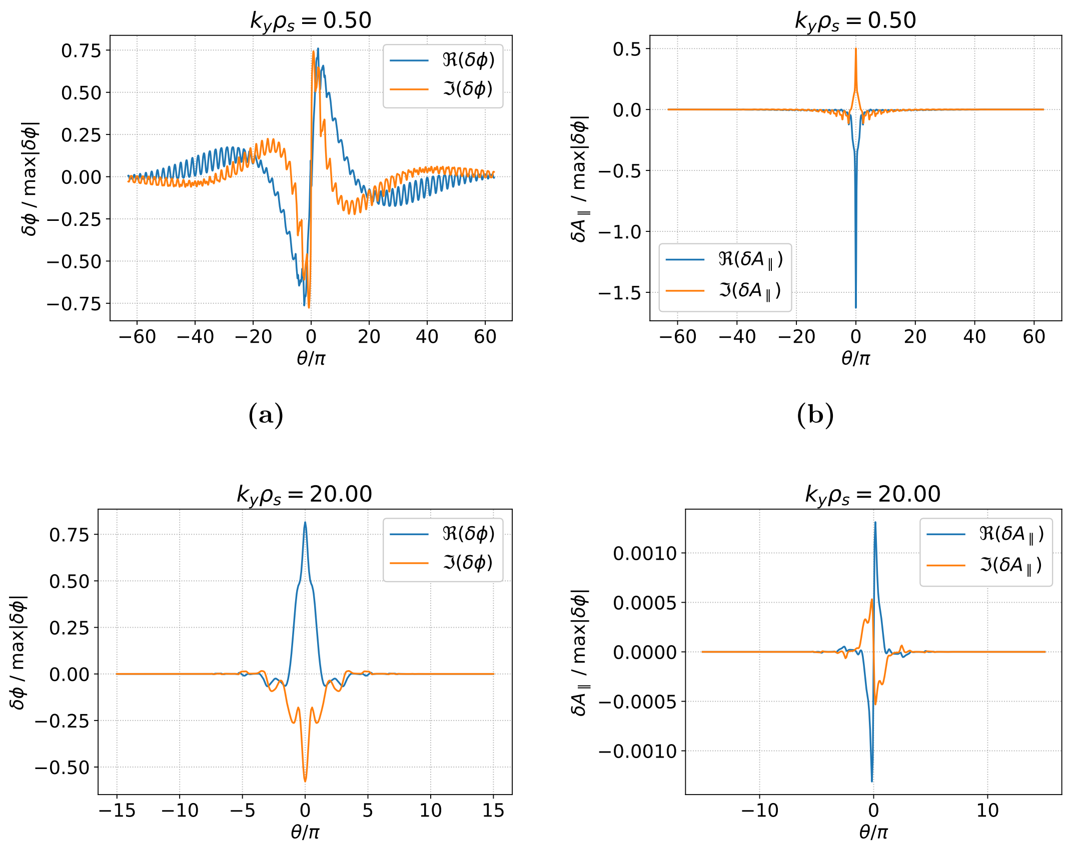

(c) **(d)**

Figure 3: *Real and imaginary part of $\delta\phi/\max|\delta\phi|$ [(a) and (c)] and $\delta A_\parallel/\max|\delta\phi|$ [(b) and (d)] as a function of the ballooning angle at the two k_y values corresponding to the maximum growth rate of the ion and electron scale instabilities.*

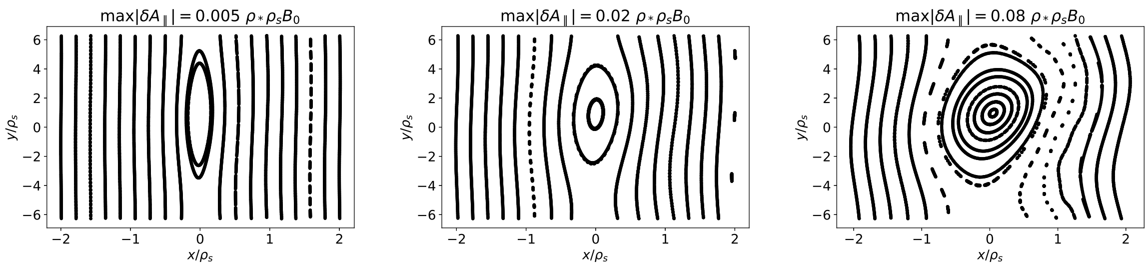

(a) **(b)** **(c)**

Figure 4: *Poincare map of the magnetic field lines in the proximity of a rational surface (centered at $x = 0$ here) showing the formation of a magnetic island caused by the MTM instability at $k_y\rho_s = 0.5$. Panels (a), (b) and (c) correspond to different amplitudes of $\delta A_\parallel$.*

Since $\nu_e \simeq \omega$, this MTM instability sits between the collisionless and semi-collisional regimes of Ref. [7]. This regime has been numerically studied in Ref. [8] and analytically addressed in a recent work reported in Ref. [31]. Both works show that the growth rate of MTMs strongly depends on the electron collision frequency. The collisionality in the MAST reference case is $\nu_* = \nu_e qR/(\epsilon^{3/2}v_{\mathrm{th,e}}) \simeq 0.1$, with $\epsilon = r/R$ the inverse aspect ratio. Therefore, trapped electron effects may also provide an additional drive for the MTM instability, as described in Ref. [10].

The tearing instability leads to the formation of magnetic islands. Fig. 4 shows a Poincaré map of the magnetic field at three different amplitudes of $\delta A_\parallel$ at $k_y\rho_s = 0.5$, which corresponds to the most unstable MTM. We highlight that the amplitude of $\delta A_\parallel$ used in Fig. 4 is chosen only for representative purposes, as the actual value of $\delta A_\parallel$ for a linear unstable mode grows exponentially until nonlinear effects cause saturation. The magnetic island forms at a rational surface located at $x = 0$. We note from Fig. 4 that the magnetic island width increases from $w_{\mathrm{island}} \simeq 0.5\,\rho_s$ to $w_{\mathrm{island}} \simeq 2\,\rho_s$ as $\delta A_\parallel$ is increased from $5 \times 10^{-3}\,\rho_*\rho_s B_0$ to $8 \times 10^{-2}\,\rho_*\rho_s B_0$, which is in agreement with the prediction of Eq. (1). The distance between adjacent rational surfaces at $k_y\rho_s = 0.5$ is given by Eq. (2) and it is $\Delta r = 1/(sk_y) \simeq 6\,\rho_s$, which is a factor of three larger than the island width at $\max|\delta A_\parallel| = 0.08$. If $\delta A_\parallel$ is further increased, the magnetic islands generated by this mode at different rational surfaces overlap partially, therefore generating a region of stochasticity. The formation of a stochastic layer can strongly enhance heat transport, as shown later in Sec. 5. We note that multiple toroidal modes are evolved in nonlinear simulations, thus reducing the distance between adjacent resonant surfaces as compared to the distance between rational surfaces for fixed n.

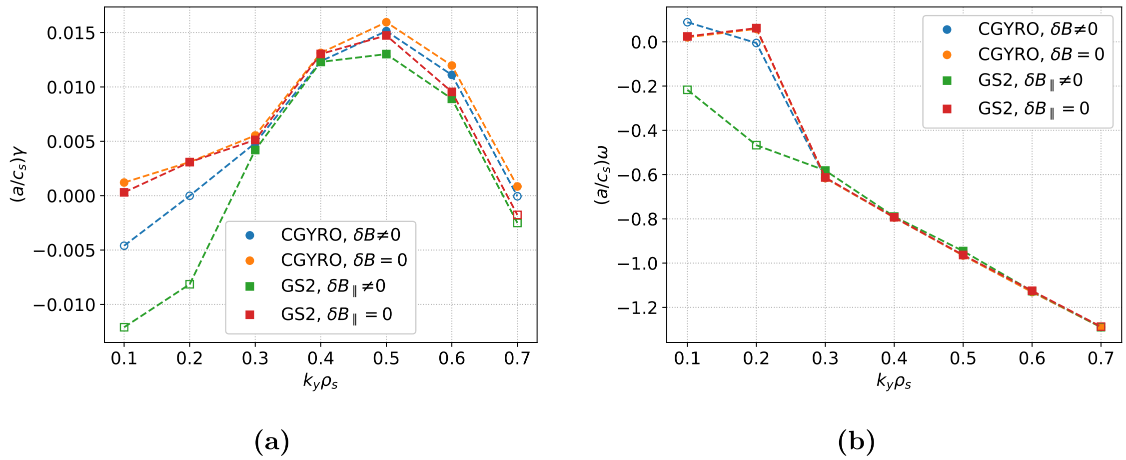

Figure 5: *Growth rate (a) and mode frequency (b) as a function of k_y from CGYRO and GS2 linear simulations with and without $\delta B_\parallel$. Unstable and stable modes are shown with solid and open markers, respectively.*

3. Linear characterisation of the MTM instability

We explore here the sensitivity of the MTM instability to various parameters and, in particular, to the electron collision frequency. Linear simulations are carried out with the gyrokinetic codes CGYRO [32] and GS2, using a similar numerical resolution in the two codes, as reported in table 2. A benchmark of the reference case is shown in Fig. 5, where linear simulations with and without $\delta B_\parallel$ are considered. A good agreement between CGYRO and GS2 growth rate and mode frequency values is observed in the region $0.2 < k_y\rho_s < 0.7$ where MTMs are unstable. We note that the MTM instability is weakly affected by $\delta B_\parallel$, in agreement with Ref. [14]. The modes at $k_y\rho_s \leq 0.2$ are stable when $\delta B_\parallel \neq 0$ and unstable when $\delta B_\parallel = 0$. Therefore, parallel magnetic fluctuations are important to suppress this low k_y ion temperature gradient (ITG) instability‡. Parallel magnetic fluctuations are retained in all the following linear and nonlinear simulations, and therefore the ITG mode at low k_y is stable.

The effect of the electron temperature gradient is investigated in Fig. 6, where growth rate and mode frequency values are shown at different values of a/L_{T_e}. The growth rate depends on the electron temperature gradient, as predicted by early analytical works [1, 9]. We note that the dependence on a/L_{T_e} is non-monotonic and the maximum growth rate is reached at the reference value of a/L_{T_e}. A non-monotonic dependence has also been observed in previous MAST linear simulations, as shown in Ref. [14], where a resonance mechanism occurring at $\nu_e \simeq \omega$ is proposed as a possible explanation, as well as in ASDEX Upgrade and JET linear gyrokinetic simulations [23]. In addition, we also show in Fig. 6 the growth rate value from linear simulations with

‡ This instability is observed in the electrostatic limit and has a mode frequency in the ion diamagnetic direction (positive sign).

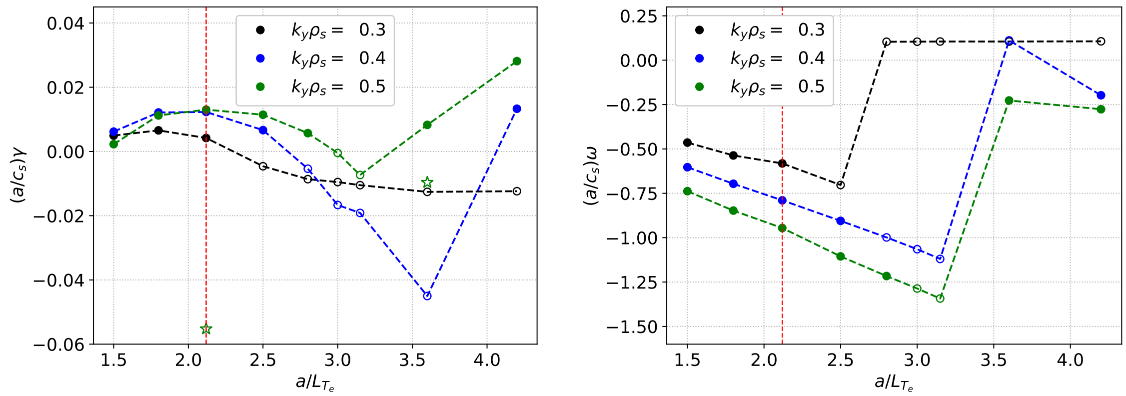

Figure 6: *Growth rate (a) and mode frequency (b) as a function of the temperature gradient at three different values of k_y. Unstable and stable modes are shown with solid and open markers, respectively. The star markers represent simulations with adiabatic passing and kinetic trapped electrons at $k_y\rho_s = 0.5$ with $a/L_{T_e} = 2.1$ (nominal value) and $a/L_{T_e} = 3.6$. The red vertical dashed line corresponds to the reference value of a/L_{T_e}. Results from GS2 linear simulations.*

adiabatic passing electrons and kinetic trapped electrons at two different values of a/L_{T_e}. We note that these modes are stable when adiabatic passing electrons are considered, hence pointing out a minor role played by trapped electrons.

Fig. 6 shows that MTMs are stable at intermediate a/L_{T_e} values, while another instability appears at large a/L_{T_e}, associated with a transition in the mode frequency, which, however, remains in the electron diamagnetic direction. The eigenfunctions corresponding to the mode at $k_y\rho_s = 0.5$ and $a/L_{T_e} = 4.2$ are shown in Fig. 7. The electrostatic potential is very elongated in the ballooning angle, similarly to the MTM instability. On the other hand, the mode has a twisting parity ($\delta\phi$ is even and $\delta A_\parallel$ odd), it is unstable also in the electrostatic limit and it is driven unstable by kinetic passing electrons, as shown in Fig. 6. The instability appearing at large a/L_{T_e} is a ETG mode characterised by $k_y\rho_s \sim 1$ and $k_x\rho_s > 1$, which is similar to the long wavelength ETG instability described in Ref. [33] (see Appendix C for further details on this instability).

The results of a density gradient scan are presented in Fig. 8, where the growth rate and mode frequency at different k_y values are shown as a function of a/L_n. The growth rate decreases as the density gradient increases, similarly to the linear simulations in Ref. [24].

The effect of the electron collision frequency is investigated in Fig. 9, where growth rate and frequency values are shown at various values of ν_e and k_y. The MTM instability is suppressed at low collisionality in favour of ITG (at low k_y) and ETG (at high k_y), thus confirming the collisional nature of this MTM instability, which is stable in the collisionless limit. The MTM growth rate increases with ν_e, until it reaches its maximum

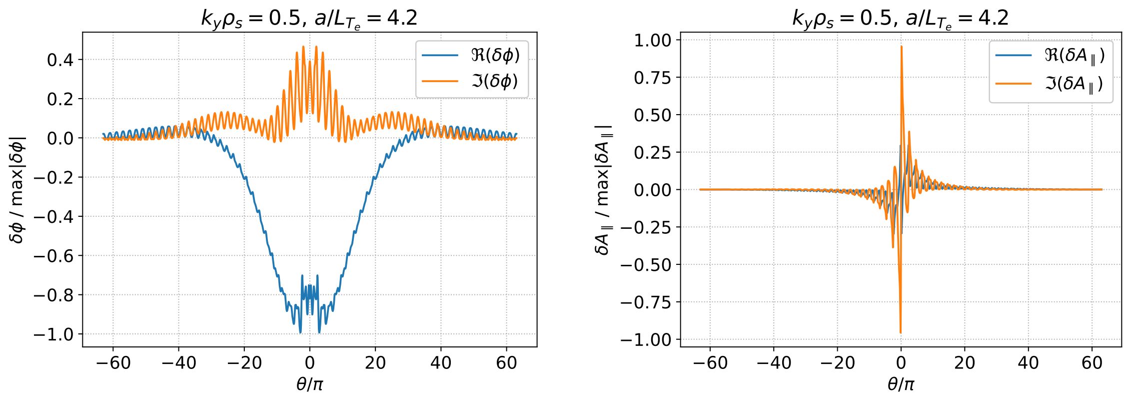

(a) **(b)**

Figure 7: *Real and imaginary part of $\delta\phi$ (a) and $\delta A_\parallel$ (b) corresponding to the unstable mode at $k_y\rho_s = 0.5$ and $a/L_{T_e} = 4.2$.*

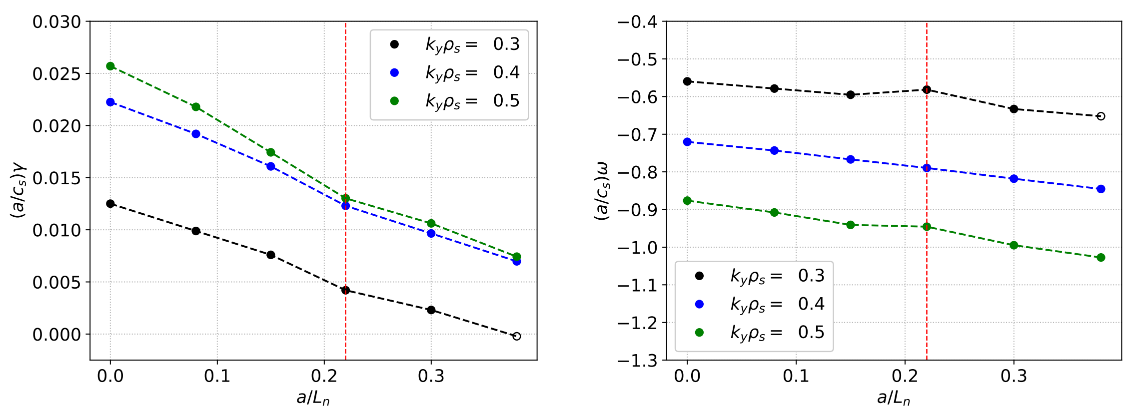

(a) **(b)**

Figure 8: *Growth rate (a) and mode frequency (b) as a function of the density gradient at three different values of k_y. Unstable and stable modes are shown with solid and open markers, respectively. The red vertical dashed line corresponds to the reference value of a/L_n. Results from GS2 linear simulations.*

value around $\nu_e = 0.42\ c_s/a$. At this value of collision frequency, which is approximately half the value of the collision frequency of the reference case, the growth rate is a factor of two larger than in the reference case. The growth rate value decreases when the collisionality is further increased. Since the maximum growth rate occurs at $\nu_e \simeq \omega_{*e}$, with ω_{*e} the diamagnetic electron frequency, this may suggest a resonance mechanism similar to the one observed in the electron temperature scan. We note that the ITG instability is suppressed when $\nu_e > 0.4\ c_s/a$, while the onset of the ETG instability shifts at higher k_y values when ν_e is increased (see Appendix C for further details). In the following, we consider the most unstable case at $\nu_e = 0.42\ c_s/a$. A comparison

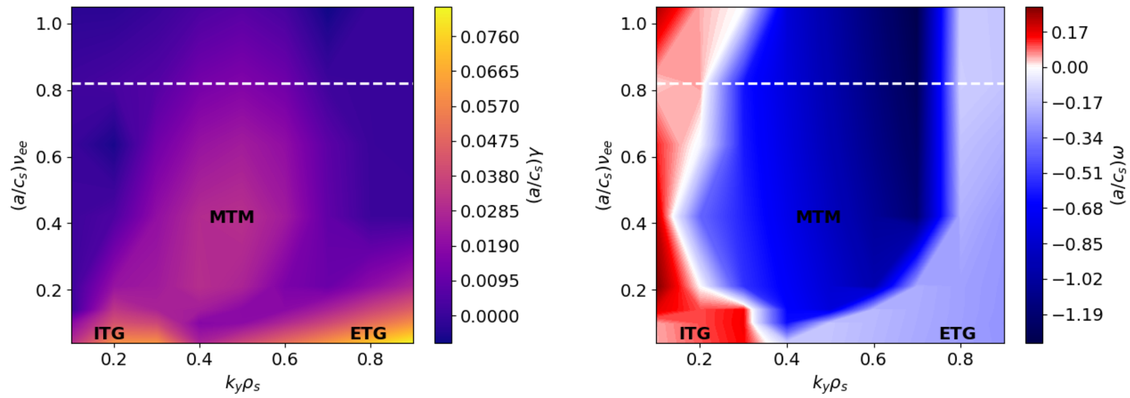

(a) **(b)**

Figure 9: *Growth rate (a) and mode frequency (b) as a function of k_y and ν_e. The white dashed horizontal line indicates the value of ν_e in the reference MAST case. Results from CGYRO linear simulations.*

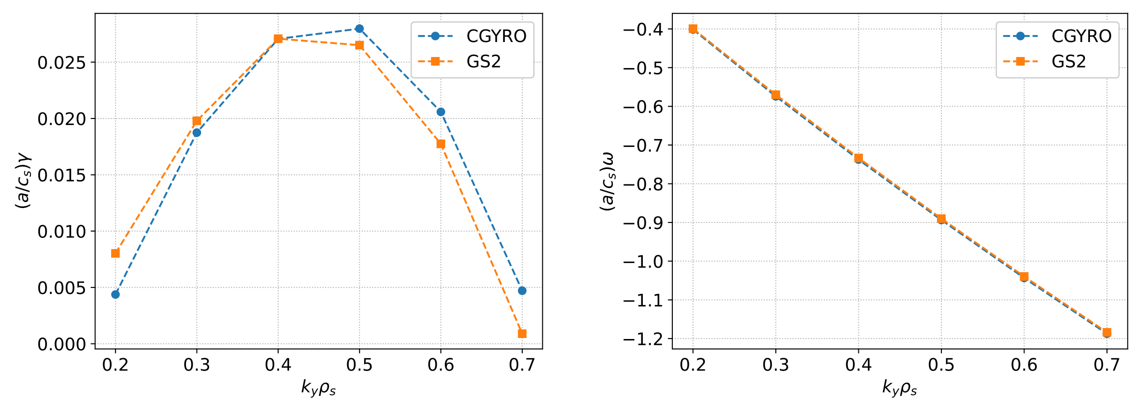

(a) **(b)**

Figure 10: *Comparison between CGYRO and GS2 growth rate (a) and mode frequency (b) from linear simulations with $\nu_e = 0.42\, c_s/a$. Only unstable modes are shown.*

between CGYRO and GS2 linear simulations at $\nu_e = 0.42\ c_s/a$ is shown in Fig. 10. A good agreement is observed over the entire k_y range both in the growth rate and mode frequency values.

The driving mechanism of the MTM instability of Ref. [1] requires a velocity dependent collision frequency [9]. In Fig. 11, we compare the results of linear simulations with and without a velocity dependence in the collisional operator. The MTM instability is retrieved only when the velocity dependence is retained. Modes at $k_y\rho_s > 0.1$ are stable when $\nu_e(v) = \nu_e(v_{\mathrm{th,e}})$. The mode at $k_y\rho_s = 0.1$ is stable in the reference case and unstable when an energy independent collision operator is considered. As an aside, we note that the MAST linear simulations of Ref. [14] show a collisional MTM instability

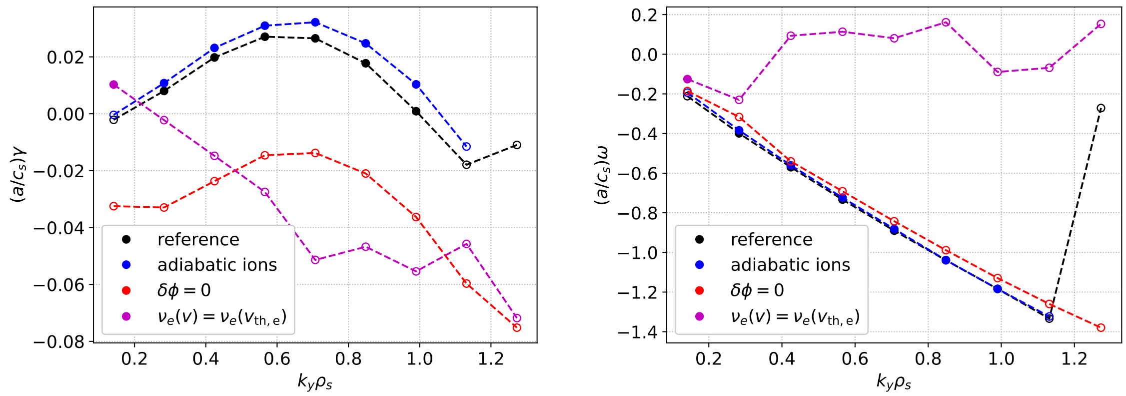

(a) **(b)**

Figure 11: *Growth rate (a) and mode frequency (b) as a function of k_y from GS2 linear simulations at $\nu_e = 0.42\, c_s/a$ with adiabatic ions (blue line), with $\delta\phi = 0$ (red line) and with a velocity independent collision frequency (magenta line). Solid and open markers are used for unstable and stable modes, respectively.*

even when a velocity independent collisional operator is used, therefore suggesting a qualitatively different MTM instability.

Previous analytical works suggest also an important stabilising effect on the MTM instability from the ion dynamics [11]. Results of linear simulations with adiabatic ions are shown in Fig. 11. Growth rate values increase slightly when considering adiabatic ions, so the stabilising effect from kinetic ions is very weak in the case considered here.

Finally, the dependence on the electrostatic potential fluctuations is investigated. Fig. 11 shows that MTMs are stable in the simulation with $\delta\phi = 0$, i.e. electrostatic potential fluctuations are essential for the drift-tearing mode to be unstable in this case. This is in agreement with the numerical calculations of Ref. [8] and the theoretical predictions of Ref. [31], while it contrasts with previous MAST linear simulations [14], where a weaker dependence of MTMs growth rate values on electrostatic potential fluctuations is observed. The theoretical analysis in Ref. [7] predicts an important effect of electrostatic potential fluctuations in the collisional regime.

4. Nonlinear simulation results and saturation mechanism

We present here the results of a nonlinear simulation scan carried out by using CGYRO. These nonlinear simulations are computationally quite expensive since a high numerical resolution is required to properly resolve the MTM instability, especially in the radial direction (see table 3).

Fig. 12 (a) shows the time trace of the total heat flux from nonlinear simulations with different values of $a\nu_e/c_s \in \{1.05, 0.82, 0.63, 0.42, 0.21\}$. The value of the electron collision frequency in the MAST reference case is $\nu_e = 0.82\ c_s/a$. The linear scan

CGYRO nonlinear simulations			
Parameters	Reference	Lower $k_{y,\min}$	Higher s
n_θ	32	32	32
n_r	256	256	256
n_{k_y}	10	20	16
n_ξ	24	24	24
n_ϵ	8	8	8
$k_{y,\min}\rho_s$	0.07	0.035	0.035
L_x/ρ_s	168	168	82

Table 3: *Numerical resolution used in CGYRO nonlinear simulations. The quantities n_{ky}, $k_{y,\min}$ and L_x represent the number of evolved k_y modes, the minimum evolved finite k_y value and the radial extension of the flux tube domain, respectively. The simulation "higher s" is discussed in Sec. 5.*

presented in the previous section shows that the maximum MTM growth rate is achieved at approximately $\nu_e \simeq 0.42\ c_s/a$. We note that the heat flux driven by MTMs is negligible for $\nu_e > 0.6\ c_s/a$, despite MTMs being linearly unstable (see Fig. 9). Therefore, there is no contribution to the heat flux from the MTM instability in the reference MAST case (most of the turbulent heat flux is driven by the ETG instability as shown in Appendix B). Fig. 12 (b) shows the electromagnetic and electrostatic contribution to the saturated heat flux at different values of electron collision frequency. When ν_e decreases from $0.63\ c_s/a$ to $0.42\ c_s/a$, the heat flux increases by an order of magnitude, while the maximum growth rate of the linear MTM instability increases by less than a factor two. At $\nu_e = 0.42\ c_s/a$ and $\nu_e = 0.21\ c_s/a$, the heat flux saturates approximately at $Q_{\text{tot}} \simeq 0.02\ Q_{gB}$, where $Q_{gB} = \rho_*^2 n_e T_e c_s$ is the gyro-Bohm heat flux, corresponding to $Q_{\text{tot}} \simeq 0.002$ MW/m^2. We note that the heat flux at $\nu_e < 0.6\ c_s/a$ saturates at a value that is more than a factor of two than the saturated heat flux driven by the ETG instability in the MAST reference case (see Appendix B). Fig. 12 (b) shows that the electromagnetic heat flux largely dominates over the electrostatic contribution, in agreement with previous nonlinear gyrokinetic simulations of MTMs [2, 3]. In the following, we consider the case with $\nu_e = 0.42\, c_s/a$.

The sensitivity to some numerical parameters is investigated by carrying out a set of nonlinear simulations with different parallel grid resolution, different values of $k_{y,\min}$ (the minimum finite k_y mode evolved in the simulation) and different size of the radial flux-tube domain. The saturated heat flux level for each of these simulations is shown in Fig. 13. The simulation with half the number of points in the parallel direction predicts the same heat flux value within the error bar. Also the simulation with $k_{y,\min} = k_{y,\min,\text{ref}}/2$ predicts the same heat flux level within the error bar. On the other hand, the simulation with $k_{y,\min} = 2k_{y,\min,\text{ref}}$ predicts a much lower heat flux. This is partially expected as modes at $k_y\rho_s \simeq 0.2$ are MTM unstable. The importance of

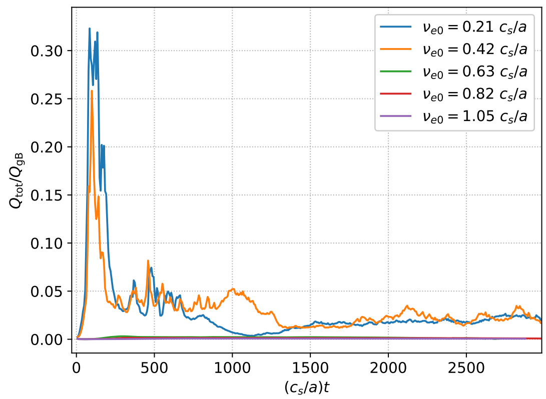

(a)

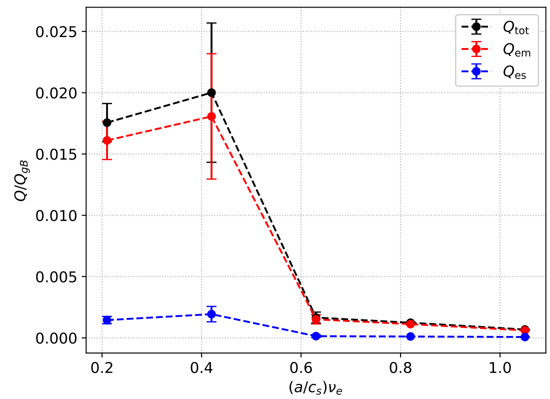

(b)

Figure 12: *(a) Time trace of total heat flux from CGYRO nonlinear simulations with different values of electron collision frequency. The nominal value of collision frequency in the MAST reference case is $\nu_e = 0.82\ c_s/a$, represented by the red line. (b) Saturated level of the total (black), electromagnetic (red) and electrostatic (blue) heat flux obtained by time averaging the heat flux at $t > 1500\,a/c_s$. The error bars are determined from standard deviation.*

low k_y modes is highlighted in Fig. 14, where $|\delta\phi(k_x, k_y)|^2$ and $|\delta A_\parallel(k_x, k_y)|^2$ spectra are shown as a function of k_x and k_y. The maximum value of $|\delta\phi(k_x, k_y)|^2$ and $|\delta A_\parallel(k_x, k_y)|^2$ occurs at $k_y\rho_s \simeq 0.15$ and small k_x values§. In the simulation with $k_{y,\min} = 2k_{y,\min,\mathrm{ref}}$, the $|\delta\phi(k_x, k_y)|^2$ and $|\delta A_\parallel(k_x, k_y)|^2$ spectra are under resolved and the heat flux is therefore underestimated. We note that by varying $k_{y,\min}$ the spacing between adjacent rational surfaces is modified and this may potentially affect the formation of stochastic layers due to magnetic island overlapping, as discussed in Sec. 5, thus also partially explaining why the simulation with $k_{y,\min} = 2k_{y,\min,\mathrm{ref}}$ predicts a much smaller heat flux value.

The $\delta\phi$ spectrum peaks at low k_y values and is extended in k_x [see Fig. 14 (a)], i.e. significant $\delta\phi$ amplitude is observed at high k_x. The electrostatic potential fluctuations are therefore very narrow radially and elongated in the binormal direction, as shown in Fig. 15 (a). On the opposite, the $\delta A_\parallel$ spectrum is more narrow in k_x [see Fig. 14 (b)], thus resulting in much longer radial perturbations, as shown in Fig. 15 (b), which remain, however, smaller than the radial size of the flux tube domain. Given the presence of elongated $\delta A_\parallel$ structures, the effect of the radial extension of the flux tube domain is tested. Fig. 13 shows that no significant difference on the heat flux level is observed in the simulation with $L_x = L_{x,\mathrm{ref}}/2$. This is also expected from Fig. 15 (b), where the radial extension of $A_\parallel$ fluctuations is considerably smaller than the radial size of the flux tube domain, which therefore could be reduced by a factor of two without affecting

§ Large mode amplitudes at low k_x values correspond to radially extended perturbations that may question the applicability of the local approximation. On the other hand, Fig. 15 shows that the radial extension of $\delta\phi$ and $\delta A_\parallel$ is considerably smaller than the radial size of the flux tube domain.

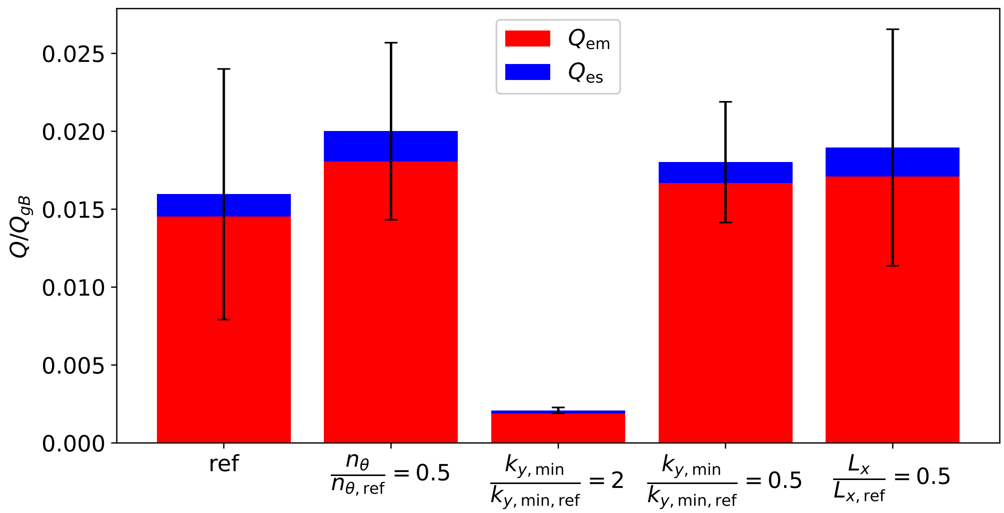

Figure 13: *Saturated heat flux value from CGYRO nonlinear simulations at* $\nu_e = 0.42\,c_s/a$ *and modified numerical resolution or domain size. The numerical resolution used in the reference nonlinear simulation is listed in table 3. The error bar on the total heat flux is determined from standard deviation.*

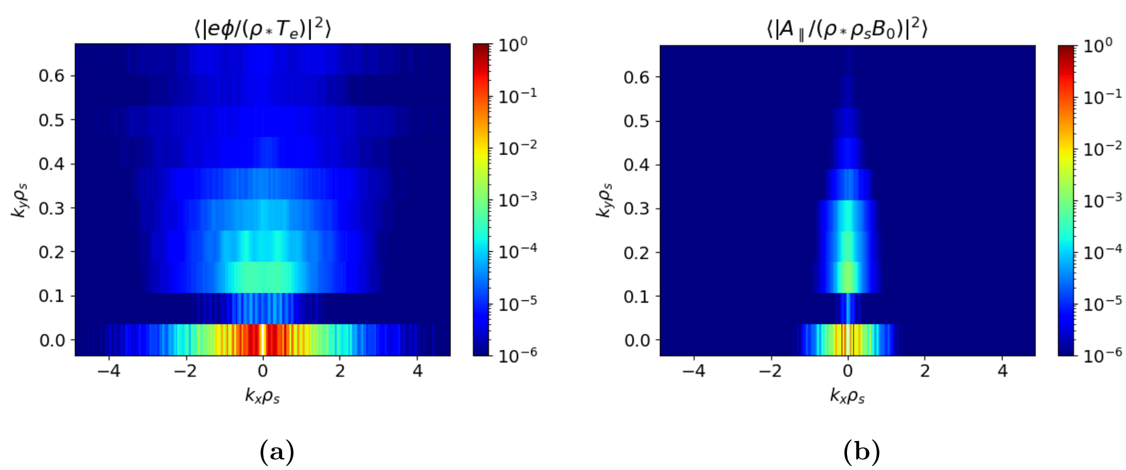

Figure 14: *Spectrum of* $\delta\phi$ *(a) and* $\delta A_\parallel$ *(b) averaged over* $t \in [1500, 2500]\,a/c_s$ *and* θ *from the nonlinear simulation at* $\nu_e = 0.42\,c_s/a$.

the radial resolution of $\delta A_\parallel$. We note that, because of the low magnetic shear and $k_{y,\mathrm{min}}$ values, the L_x and L_y values used here are comparable to the size of MAST. This questions the applicability of the local approximation and global gyrokinetic simulations may be required to accurately predict the MTM driven heat flux, which is outside the scope of the present work in which we are interested in the saturation of MTMs within the local gyrokinetic framework.

The $|\delta\phi(k_x, k_y)|^2$ and $|\delta A_\parallel(k_x, k_y)|^2$ spectra in Fig. 14 reveal the presence of a very

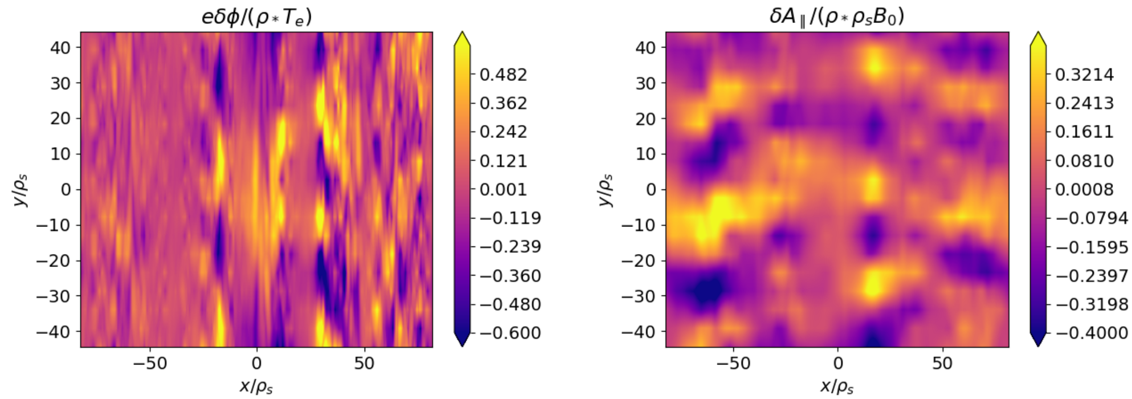

(a) **(b)**

Figure 15: *Snapshot of* $\delta\phi$ *(a) and* $\delta A_\parallel$ *(b) from the nonlinear simulation with* $\nu_e = 0.42\, c_s/a$. *Fluctuating quantities are shown without their zonal component.*

strong zonal component, which is more than an order of magnitude higher than the largest non zonal $\delta\phi$ and $\delta A_\parallel$ modes. Zonal flows and/or zonal fields may therefore provide an important saturation mechanism here. In particular, the perturbed magnetic shear from zonal $A_\parallel$ perturbations, $\tilde{s} = qR/B(\mathrm{d}\delta B_y/\mathrm{d}x) \simeq 0.1$, is comparable to the local magnetic shear, $s = 0.34$, thus suggesting a potential important role of zonal fields. Saturation occurs via nonlinear interaction, where the nonlinear source term in the gyrokinetic equation can be written as [32]

$$S_{a,\mathrm{NL}} = [\chi_a, h_a] = \frac{\partial \chi_a}{\partial x}\frac{\partial h_a}{\partial y} - \frac{\partial h_a}{\partial x}\frac{\partial \chi_a}{\partial y}\,, \tag{4}$$

where x and y are the radial and binormal coordinates, h_a is the non adiabatic perturbed distribution function of species a, and the generalised field potential

$$\chi_a = \Big\langle \delta\phi(\mathbf{R}+\boldsymbol{\rho}) - v_\parallel \delta A_\parallel(\mathbf{R}+\boldsymbol{\rho}) - \mathbf{v}_\perp \cdot \delta\mathbf{A}_\perp(\mathbf{R}+\boldsymbol{\rho}) \Big\rangle_{\mathbf{R}}\,, \tag{5}$$

with $\mathbf{R}$ the guiding-center position, $\boldsymbol{\rho} = \mathbf{b}\times\mathbf{v}/\Omega_{ca}$ and $\langle\cdot\rangle_{\mathbf{R}}$ denotes the gyro-average (see Ref. [32] for details). Different simulation tests are carried out to investigate the effect of $\langle\delta\phi(k_x, k_y = 0)\rangle_\theta$ and $\langle\delta A_\parallel(k_x, k_y = 0)\rangle_\theta$ in the nonlinear term of Eq. (4). The time trace of the total heat flux from these tests is shown in Fig. 16. Removing $\langle\delta\phi(k_x, k_y = 0)\rangle_\theta$ in Eq. (4) has little effect on the saturated heat flux level, thus excluding an important effect of zonal flows on the saturation mechanism. On the other hand, removing $\langle\delta A_\parallel(k_x, k_y = 0)\rangle_\theta$ leads to a substantial increase of the heat flux, pointing out the main role played by zonal fields, in agreement with Ref. [6].

The k_x spectrum of the zonal fields, $\langle A_\parallel(k_x, k_y = 0)\rangle_\theta$, and its shear, $\langle k_x^2 A_\parallel(k_x, k_y = 0)\rangle_\theta$, are shown in Fig. 17 in the proximity of $k_x = 0$. We note that the zonal $A_\parallel$ spectrum peaks approximately at $|k_x\rho_s| \simeq 0.15$ and decays quickly as $|k_x|$ increases. The shear of the zonal fields shows a broader k_x spectrum, with its maximum value occurring in the region between $|k_x\rho_s| \simeq 0.15$ and $|k_x\rho_s| \simeq 0.3$. Therefore, we expect

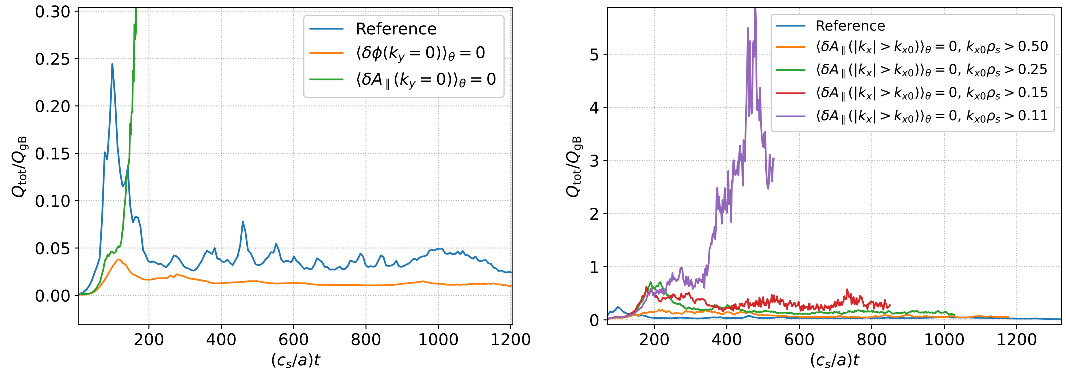

(a) **(b)**

Figure 16: *(a) Time trace of the total heat flux from nonlinear tests where the zonal flows or zonal fields nonlinear interaction is turned off. The blue line represents the reference simulation ($\nu_e = 0.42\, c_s/a$), the orange line represents a test with $\langle\delta\phi\rangle_\theta = 0$ and the red line a test $\langle\delta A_\parallel\rangle_\theta = 0$ in the nonlinear source term [see Eq. (4)]. (b) Nonlinear simulation tests with $\langle\delta A_\parallel(|k_x| > k_{x0})\rangle_\theta = 0$ in the nonlinear source term for various values of k_{x0}.*

an important role played by the low k_x zonal field modes on the saturation mechanism. The effect of the low k_x zonal field modes on the heat flux is tested in Fig. 16 (b) by removing $\langle\delta A_\parallel(k_x > k_{x0})\rangle_\theta$ in Eq. (4) with different values of k_{x0}. The saturated heat flux value is controlled by the value of k_{x0}. The heat flux increases when the zonal field modes with $|k_{x0}\rho_s| \geq 0.25$ are removed, which is consistent with a reduction of the zonal fields shear. We note that a transition to very large heat flux values is observed only when the zonal field modes with $|k_{x0}\rho_s| > 0.11$ are removed from the nonlinear source term. We also mention that removing the zonal $A_\parallel$ modes with $|k_x\rho_s| \leq 0.11$ while retaining the modes with $|k_x\rho_s| > 0.11$ causes a transition to large heat flux values, thus confirming the important of the low k_x zonal $A_\parallel$ modes. As a consequence, the zonal fields saturation mechanism is effective only if the low k_x spectrum is well resolved (at least in this case where both the zonal fields and the corresponding shear peak at low k_x), which translates into a domain sufficiently extended in the radial direction. Fig. 17 shows that the maximum of $\langle\delta A_\parallel\rangle_\theta$ and $\langle k_x^2\delta A_\parallel\rangle_\theta$ spectra is well resolved in simulations with $L_x = L_{x,\mathrm{ref}}$ and $L_x = L_{x,\mathrm{ref}}/2$. On the other hand, the resolution is relatively low in a simulation with $L_x = L_{x,\mathrm{ref}}/4 = 1/(sk_{y,\mathrm{min}})$, which is the minimum L_x value that can be considered keeping all other parameters fixed. This simulation is affected by heat flux oscillations and convergence difficulties. The k_x resolution is therefore important here to correctly capture the saturation mechanism via zonal fields.

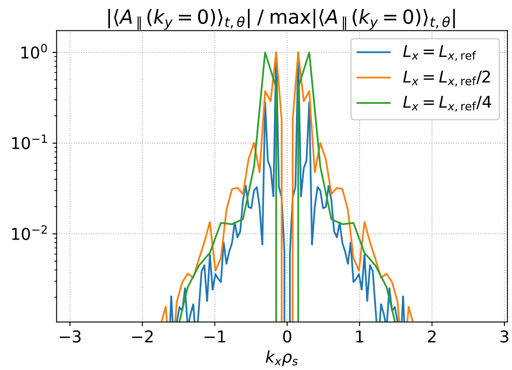

(a)

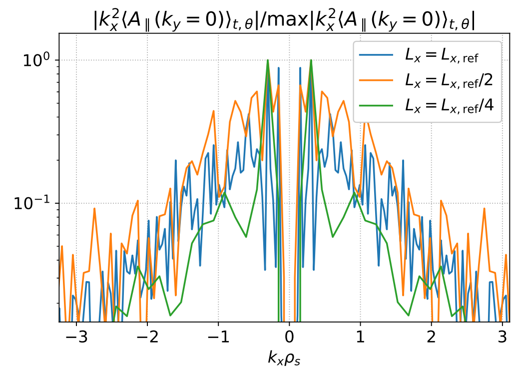

(b)

Figure 17: *Normalised zonal fields (a) and zonal fields shear (b) averaged over time and θ as a function of k_x in the proximity of $k_x = 0$ from nonlinear simulations at $\nu_e = 0.42\, c_s/a$ with different radial domain extensions.*

5. Magnetic islands interaction and local shear effect

We analyse here the effect of magnetic islands overlapping and subsequent formation of a stochastic layer. Fig. 18 shows a Poincaré map of the magnetic field on a radial section of the flux tube domain generated from the reference nonlinear simulation with $\nu_e = 0.42\ c_s/a$. Several magnetic islands with different mode numbers can be clearly distinguished. The largest island width corresponds to the mode at $k_y/k_{y,\min} = 2$, in agreement with the $\delta A_\parallel$ spectrum shown in Fig. 14, where the largest $\delta A_\parallel$ amplitude is achieved at $k_y/k_{y,\min} = 2$ (excluding the zonal component). The island width is smaller at higher k_y and the subsequent perturbation of the equilibrium magnetic field is weaker. Since the island separation is proportional to $1/n^2 \propto 1/k_y^2$ (see Eq. 3), the effect of these high-k_y islands can nonetheless be important, especially when several islands at different values of k_y overlap. For example, the radial separation of resonant surfaces for the $k_y/k_{y,\min} = 5$ islands is $\Delta r = 1/(sk_y) \simeq 8.4\ \rho_s$ and these islands appear in Fig. 18 at $x \simeq 4\ \rho_s$, $x \simeq 13\ \rho_s$ and $x \simeq 21\ \rho_s$. The $k_y/k_{y,\min} = 7$ islands appear at $x \simeq 2.2\,\rho_s$, $x \simeq 8\,\rho_s$, $x \simeq 14\ \rho_s$ and $x \simeq 19.6\ \rho_s$ (not clearly visible in Fig. 18). The $k_y/k_{y,\min} = 3$ and $k_y/k_{y,\min} = 9$ islands also appear at a radial surface near $x = 14\ \rho_s$. The overlap of these magnetic islands generates a layer of stochastic magnetic field lines in proximity of $x = 14\ \rho_s$, as shown in Fig. 19 (a). We note that the stochastic layer is quite narrow in the radial direction and is surrounded by regions of weakly perturbed magnetic field. In fact, the overall magnetic field stochasticity is relatively low, with regions of well separated islands and almost unperturbed magnetic field. This is consistent with the MTM driven heat flux at $\nu_e = 0.42\ c_s/a$ (where the MTM instability is linearly most unstable) saturating at a small value.

The main role of zonal fields is to saturate the non zonal $\delta A_\parallel$ at low amplitude, thus reducing the width of the magnetic islands and therefore the stochastic layer size

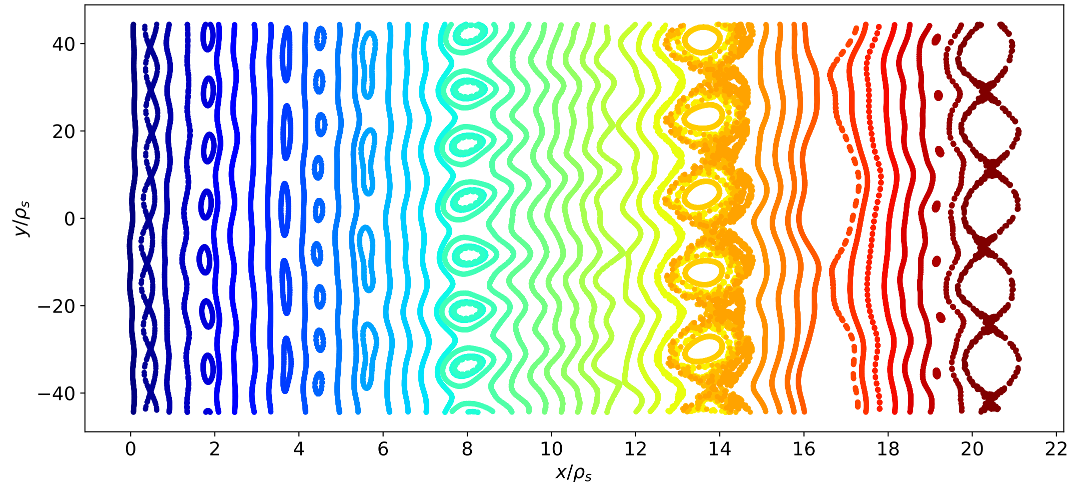

Figure 18: *Poincaré map tracing where the magnetic field crosses the outboard midplane as it winds around the torus. This is lines obtained from the nonlinear simulation with $\nu_e = 0.42\ c_s/a$. The color scale is used to identify magnetic field lines starting at the same radial position. For the sake of clarity, only a part of the flux tube radial domain is shown.*

(see Sec. 4). However, a strong zonal $A_\parallel$ can also directly affect the formation of a stochastic layer. This is shown in Fig. 19 (b), where the Poincaré map is generated without including the zonal $A_\parallel$ (the nonlinear simulation does include the zonal $A_\parallel$). By comparing Fig. 19 (a) and (b), we note that the magnetic islands at $x \simeq 12\ \rho_s$ and $x \simeq 14\ \rho_s$ merge together in the case without zonal $A_\parallel$, thus extending the radial size of the stochastic layer. We also note that the zonal $A_\parallel$ slightly shifts the radial position of rational surfaces. For example, the resonant surface with $k_y/k_{y,\min} = 5$ moves from $x \simeq 12.5$ to $x \simeq 13.5$ by adding the zonal $A_\parallel$.

Heat flux transport caused by stochastic magnetic field lines depends on both the size of magnetic islands and the separation between adjacent resonant surfaces. The island width is estimated from $\delta A_\parallel$ using Eq. (1), while the minimum separation between adjacent resonant surfaces is given by Eq. (3). By following Refs. [2, 17], we compare in Fig. 20 (a) w_{island} and δr from the nonlinear simulation at $\nu_e = 0.42\ c_s/a$. We note that δr is larger than w_{island} at all the k_y modes evolved in the nonlinear simulations, in agreement with the low level of field lines stochasticity shown in Fig. 18.

The resonant radial surface spacing is inversely proportional to the magnetic shear. Therefore, a larger stochastic layer is expected to form at higher magnetic shear. We consider therefore an additional case at higher magnetic shear, $s = 2s_{\text{ref}} \simeq 0.7$. The growth rate as a function of k_y in this new case is shown in Fig. 21. The maximum growth rate of the MTM instability is higher than in the reference case with $s = 0.34$ and it occurs at a lower k_y value. A nonlinear simulation at higher s is carried out with the numerical resolution listed in table 3. A lower value of $k_{y,\min}$ is used here

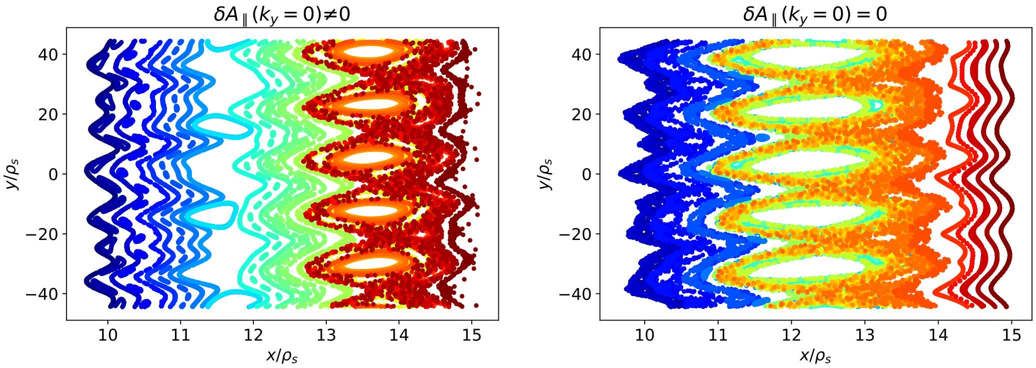

(a) **(b)**

Figure 19: *Poincaré map of a thin radial layer of the flux tube domain generated from the nonlinear simulation with $\nu_e = 0.42\ c_s/a$. The zonal $\delta A_\parallel$ component is retained in (a) and turned off in (b) when generating the Poincaré map. The color scale is used to identify magnetic field lines starting at the same radial position.*

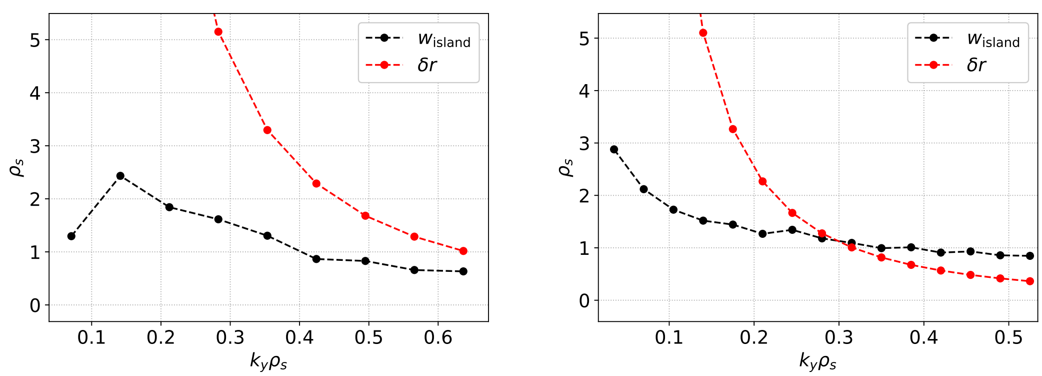

(a) $s = 0.34$ **(b)** $s = 0.7$

Figure 20: *Resonant radial surface spacing (red line) and island width (black line) as a function of k_y from the nonlinear simulations with $s = 0.34$ (a) and $s = 0.7$ (b).*

to account for the low k_y unstable modes. Fig. 20 (b) shows the comparison between $w_{\rm island}$ and δr in the simulation at higher s. The island width at different k_y values is comparable to the one from the nonlinear simulation at $s = 0.34$. In fact, the amplitude of $A_\parallel$ fluctuations from the two simulations with different magnetic shear is comparable. This is in agreement with the nonlinear MTM theory developed in Ref. [34], which predicts $|\delta B/B| \simeq \rho_e/L_{T_e} \simeq 3.5 \times 10^{-5}$ (the temperature gradient is the same in both simulations). This value is close to the one obtained from nonlinear simulations at $\nu_e = 0.42\ c_s/a$, i.e. $|\delta B/B| \simeq 6 \times 10^{-5}$. On the other hand, the resonant surface spacing is a factor two smaller in the simulation at higher s. This leads to an important qualitative change in Fig. 20 (b), where $w_{\rm island}$ is larger than δr for $k_y\rho_s > 0.3$.

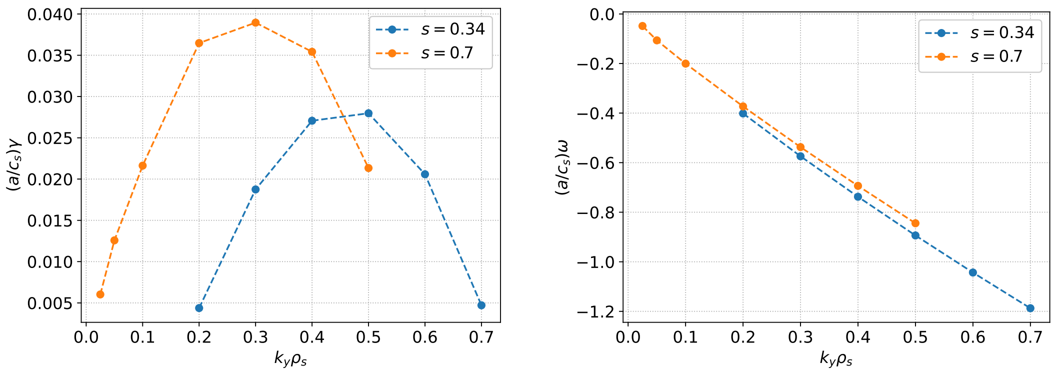

(a) **(b)**

Figure 21: *Growth rate (a) and mode frequency (b) values from CGYRO linear simulations with* $s = 0.34$ *(blue line) and* $s = 0.7$ *(orange line). Only unstable modes are shown.*

Consequently, island overlapping is more effective and a stochastic layer is expected to extend over a wider region. This is clearly shown by the Poincaré map in Fig. 22. The radial extension of the stochastic layer is much larger than in the reference case (see Fig. 18). Most of the magnetic islands visible in Fig. 18 in the low magnetic shear simulation are destroyed in the high magnetic shear simulation by the presence of a stochastic layer. Consequently, the heat flux increases in the higher magnetic shear simulation (see Fig. 23) and largely overcome the heat flux driven by the ETG instability. We note that w_{island} values in the low and high magnetic shear simulations are similar and the formation of a stochastic layer is mainly caused by a factor of four reduction of the minimum adjacent resonant surface spacing.

Following Ref. [18], a magnetic diffusion coefficient is introduced,

$$D_m = \lim_{l\to\infty} \frac{\langle [r(l) - r(0)]^2 \rangle}{2l} \simeq \lim_{l\to\infty} \frac{1}{2l}\frac{1}{N}\sum_{i=1}^{N} [r_i(l) - r_i(0)]^2 \,, \tag{6}$$

where r_i is the radial position of a field line, l is the distance along the field line and N is the number of field lines considered in the average. The magnetic diffusion coefficient converges to a well-defined value at large N. The magnetic diffusivity is computed in all the nonlinear simulations by considering the full radial extension, $N = 400$ field lines and integrating along the perturbed field line for 2000 poloidal cycles. An estimate of the electron heat transport due to stochastic magnetic field lines can be derived from D_m [17],

$$\frac{Q_{e,\text{stochastic}}}{Q_{gB}} = 2f_p\sqrt{\frac{4m_i}{\pi m_e}}\frac{a}{L_{T_e}}\left(\frac{aD_m}{\rho_s^2}\right) \tag{7}$$

where $f_p \simeq 1 - \sqrt{r/R}$ is the fraction of passing particles (magnetically trapped particles do not contribute to the stochastic transport [18]). Fig. 23 compares the electron heat

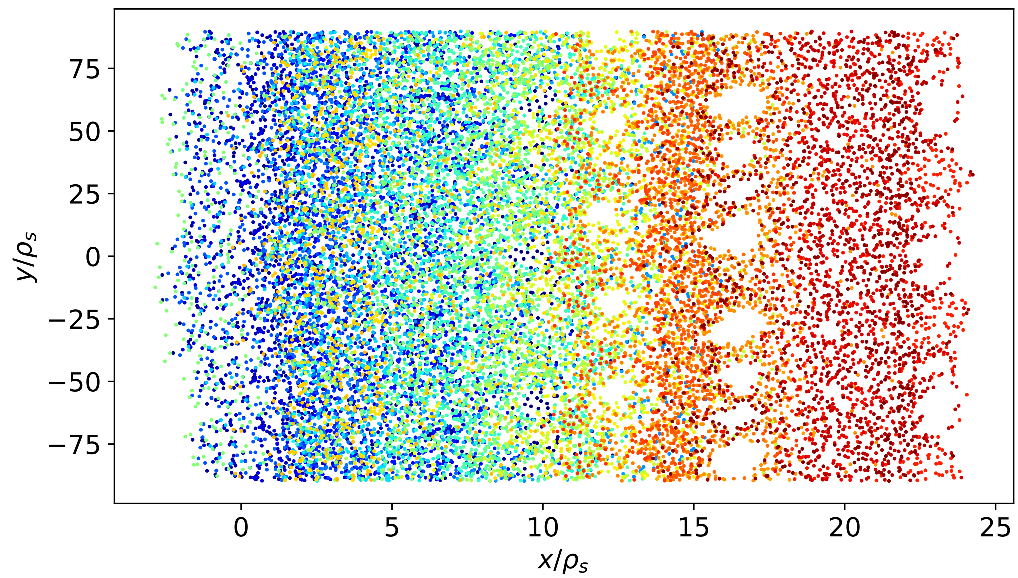

Figure 22: *Poincaré map of magnetic field obtained from the nonlinear simulation with* $\nu_e = 0.42\ c_s/a$ *and higher magnetic shear. The color scale is used to identify magnetic field lines starting at the same radial position.*

flux given by Eq. (7) to the electromagnetic electron heat flux calculated from nonlinear simulations. The trend is well reproduced and the predictions of Eq. (7) are in qualitative agreement with the heat flux predicted by nonlinear simulations. Importantly, the order of magnitude increase in the heat flux observed at higher magnetic shear is reproduced by Eq. (7). We note that the electron electromagnetic heat flux is entirely due to the stochastic magnetic diffusivity in the case of $s = 2s_{\mathrm{ref}} \simeq 0.7$, while a smaller contribution from the stochastic transport is observed in the simulations with the nominal magnetic shear value, though the stochastic contribution remains nonetheless important.

The minimum spacing between resonant surfaces depends on $k_{y,\mathrm{min}}$. Therefore, different values of $k_{y,\mathrm{min}}$ may affect the stochastic layer and the subsequent saturated heat flux level. Fig. 23 shows the stochastic heat flux in the case with $k_{y,\mathrm{min}}/k_{y,\mathrm{min,ref}} = 2.0$ and $k_{y,\mathrm{min}}/k_{y,\mathrm{min,ref}} = 0.5$. The value of $Q_{e,\mathrm{stochastic}}$ is much smaller when $k_{y,\mathrm{min}}/k_{y,\mathrm{min,ref}} = 2.0$ than in the reference case and it is significantly lower than the heat flux predicted by the nonlinear simulation. As discussed in Sec. 4, a smaller heat flux is expected as the lowest k_y unstable mode is not included in the simulation. The discrepancy between $Q_{e,\mathrm{stochastic}}$ and the electron heat flux from the simulation suggests that the stochastic magnetic diffusivity is underestimated. In fact, the minimum resonant surface spacing increases with k_y, thus reducing the magnetic island overlap. On the other hand, $Q_{e,\mathrm{stochastic}}$ agrees well with the electron heat flux from the nonlinear simulation, despite the smaller resonant surface spacing. In fact, the amplitude of $\delta A_\parallel(k_y)$ decreases as the number of k_y values increases, thus preserving the condition $w_{\mathrm{island}} < \delta r$. This comparison highlights that convergence on $k_{y,\mathrm{min}}$ should be carefully

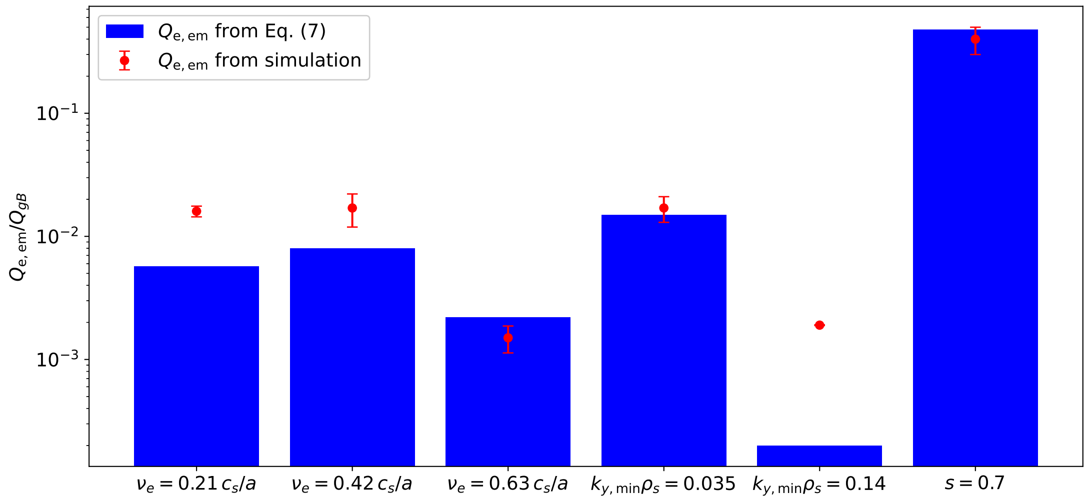

Figure 23: *Electromagnetic electron heat flux due to magnetic diffusivity (see Eq. (7)) in various nonlinear simulations with different values of electron collision frequency and* $k_{y,\min}$. *A nonlinear simulation with higher magnetic shear ($s = 0.7$) is also considered. The red markers show the saturated electromagnetic electron heat flux level computed from nonlinear simulations.*

verified when performing nonlinear MTM simulations in order to avoid a possible underestimation of the stochastic heat flux, even when all the low k_y unstable modes are included in the nonlinear simulation, especially when $w_{\text{island}} \simeq \delta r$. The condition $w_{\text{island}} \simeq \delta r$ can also be used as an indication of the importance of the MTM driven heat flux.

6. Conclusions

The MTM instability can provide significant electron heat flux transport in the high-β core of spherical tokamaks as well as in the edge of conventional aspect ratio tokamaks. An accurate prediction of MTM driven heat flux requires one to perform expensive nonlinear gyrokinetic simulations, which are often very challenging because of their numerical requirements and convergence difficulties. This motivates improved understanding of the saturation and transport mechanisms to aid the development of cheaper reduced models. In this work, linear and nonlinear gyrokinetic simulations are carried out by considering experimentally relevant scenarios built from the MAST discharge #22769, where MTMs are the dominant linear instability at $k_y\rho_s < 1$. Linear simulations show that the MTM instability is sensitive to electron temperature gradient, density gradient, magnetic shear and electron collision frequency. In the conditions of this MAST local equilibrium, MTMs carry a negligible fraction of the electron heat flux, and are stabilised by increasing ν_e above the experimental value. The MTM instability requires a velocity dependent electron collision frequency, while it is weakly affected by ion dynamics or parallel magnetic fluctuations, although including $\delta B_\parallel$ is important in order to suppress an electrostatic low k_y instability. Electrostatic potential fluctuations provide a strong destabilising mechanism. A comparison between CGYRO and GS2 linear simulations is also carried out, showing an overall good agreement both in the reference case and in a case of stronger MTM drive.

Analogously to the linear analysis, a nonlinear simulation scan in the electron collision frequency values is performed. Heat flux saturation at low heat flux is achieved at all the considered value of electron collision frequency. The heat flux driven by MTMs is negligible in the nonlinear simulation with the reference value of electron collision frequency as compared to the ETG driven heat flux, while it is an order of magnitude larger in nonlinear simulations with smaller electron collision frequency values. A strong zonal ϕ and $A_\parallel$ is observed in all the nonlinear simulations. While the effect of zonal ϕ on the saturated level of heat flux is relatively weak, a much larger heat flux is obtained when the zonal $A_\parallel$ is removed from the nonlinear source term, thus pointing out the importance of zonal fields in the saturation mechanism of this MTM instability, supporting the result of Ref. [6].

The MTM instability leads to the formation of magnetic islands at resonant surfaces. These magnetic islands can overlap if their width exceeds the radial separation between adjacent resonant surfaces, thus generating a layer of stochastic magnetic field lines. The effect of the stochastic layer formation and its radial extension on the heat flux is analysed in various nonlinear simulations. In the reference MAST case, the island widths are smaller than the minimum spacing between resonant surfaces and this is consistent with the saturation at low heat flux level. On the other hand, the heat flux increases by more than an order of magnitude when the value of the magnetic shear is doubled. In this case, the island width of large k_y modes exceeds the radial spacing between rational surfaces and a radially extended stochastic layer forms.

Heat transport caused by stochastic magnetic field lines is quantified through the magnetic diffusivity D_m given in Eq. (6). A reasonable agreement is found between the electromagnetic heat flux predicted by nonlinear simulations and the stochastic heat flux at different values of electron collision frequency and magnetic shear, thus suggesting that the MTM driven heat flux in the cases considered here is mostly due to stochastic magnetic field diffusivity and confirming the important role played by the formation of stochastic layers. The criterion $w_{\mathrm{island}} \gtrsim \delta r$ can therefore be used as an indication of saturation at non negligible MTM driven heat flux value. The saturated level of heat flux is shown to depend on the radial extension of the stochastic layer, which in turn depends on both the magnetic island width, proportional to magnetic fluctuations, and the radial separation between adjacent resonant surfaces. Nonlinear simulations with similar magnetic perturbation amplitude but different radial separation between adjacent resonant surfaces are shown to saturate at very different values.

Further work is required to derive a relation between magnetic fluctuation amplitude, adjacent resonant surfaces separation and saturated heat flux value, which will extend current quasi-linear theories (see, e.g., Ref. [35]) and lead to a very important

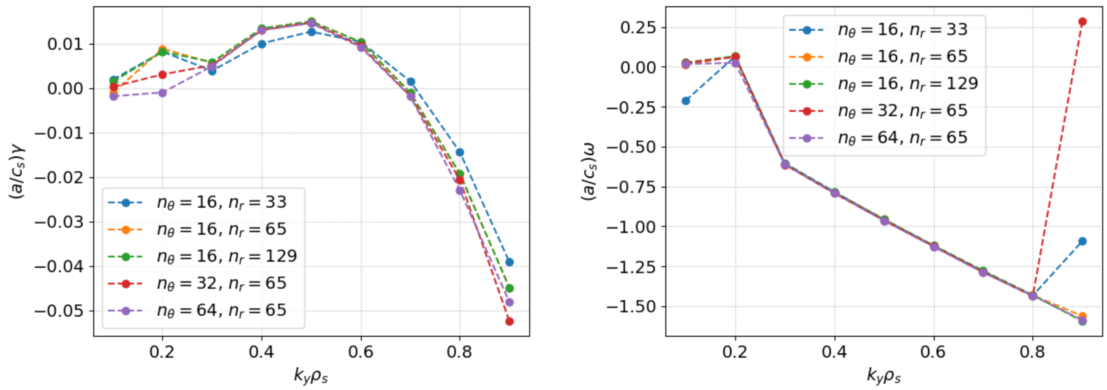

(a) **(b)**

Figure A1: *Growth rate (a) and mode frequency (b) as a function of k_y from GS2 linear simulations with $\delta B_\parallel = 0$ at different values of n_θ and n_r.*

step towards reliable and accurate MTM driven heat flux predictions from reduced models. Since the applicability of the local approximation is questionable due to the large radial extension of the flux tube domain, as imposed by the low k_y MTM instability, future work is required to investigate global effects by means of global gyrokinetic simulations.

Acknowledgements

The authors thank E. Belli, J. Candy, Ajay C. J. and H. Wilson for useful discussions. This work has been supported by the Engineering and Physical Sciences Research Council (grant numbers EP/R034737/1 and EP/W006839/1). Simulations have been performed on the ARCHER2 UK National Supercomputing Service under the project e607 and on the Viking research computing cluster at the University of York.

Appendix A. Linear convergence tests in the reference case

Linear simulations with different numerical resolution have been carried out in order to verify numerical convergence. Fig. A1 shows the growth rate and mode frequency from GS2 linear simulations performed at different values of n_θ and n_r. These tests have been performed without evolving $\delta B_\parallel$, which has a weak effect on the MTM instability (see Fig. 5). At $k_y\rho_s \geq 0.3$, convergence is achieved at $n_\theta \geq 32$ and $n_r \geq 65$, while the mode at $k_y\rho_s = 0.2$ requires a higher resolution along θ. On the other hand, this mode is not driven unstable by the MTM instability and is stable when $\delta B_\parallel \neq 0$.

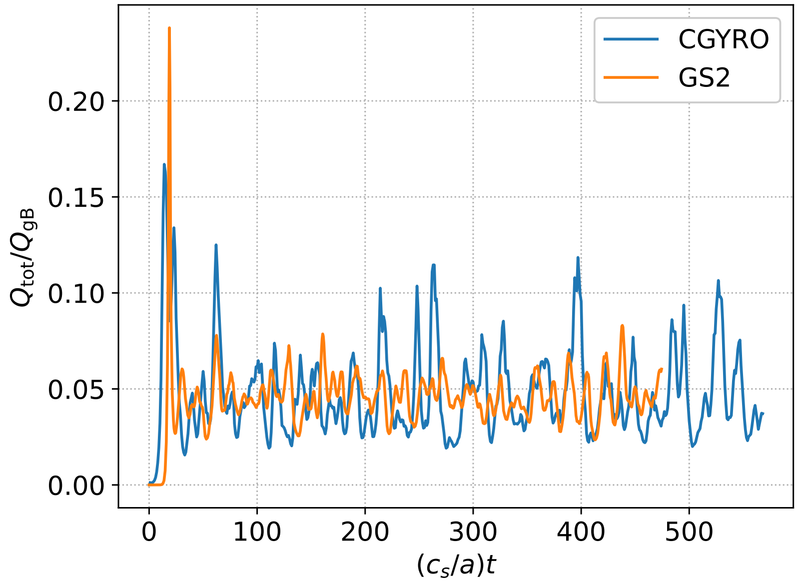

Figure B1: *Time trace of the total heat flux driven by the ETG instability in the reference MAST case. Results from CGYRO (blue line) and GS2 (orange line) nonlinear simulations.*

Appendix B. ETG driven heat flux in the reference case

The linear gyrokinetic simulations described in Sec. 2 show the presence of an ETG instability in the MAST reference case. Since the aim of this work is to investigate the mechanisms behind the MTM saturation at low heat flux level, only ion scale instability is considered. We show here that the MTM driven heat flux is negligible with respect to the ETG heat flux in this reference case at the chosen radial surface. Fig. B1 shows the time trace of the total heat flux from GS2 and CGYRO nonlinear simulations of the reference case. The heat flux saturates at $Q_{\mathrm{tot}}/Q_{gB} \simeq 0.05$, corresponding to $Q_{\mathrm{tot}} \simeq 0.01$ MW/m^2, which is of the same order of magnitude of the heat flux computed by using TRANSP code for this MAST discharge (see Fig. 2 of Ref. [21]). We highlight that the ETG heat flux is approximately two orders of magnitude larger than the MTM driven heat flux at the nominal value of electron collision frequency (see Fig. 12).

Appendix C. Binormal ion scale ETG instability

Fig. 9 shows that, when the electron collision frequency value is decreased, two different instabilities appear: an instability with positive mode frequency at $k_y\rho_s < 0.4$, which is identified as an ITG instability, and an instability with negative mode frequency at $k_y\rho_s > 0.4$, which we show here to be the electron scale ETG instability that extends into the ion scale k_y region at low electron collision frequency.

Fig. C1 shows the growth rate and the mode frequency values of unstable modes

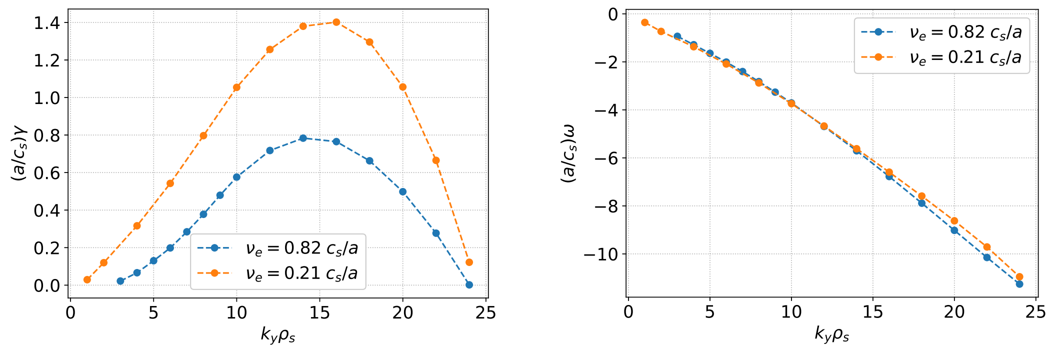

(a) **(b)**

Figure C1: *Growth rate (a) and mode frequency (b) values from GS2 linear simulations at $k_y\rho_s > 0.8$ with $\nu_e = 0.82\, c_s/a$ (reference values) and $\nu_e = 0.21\, c_s/a$. Only unstable modes are shown.*

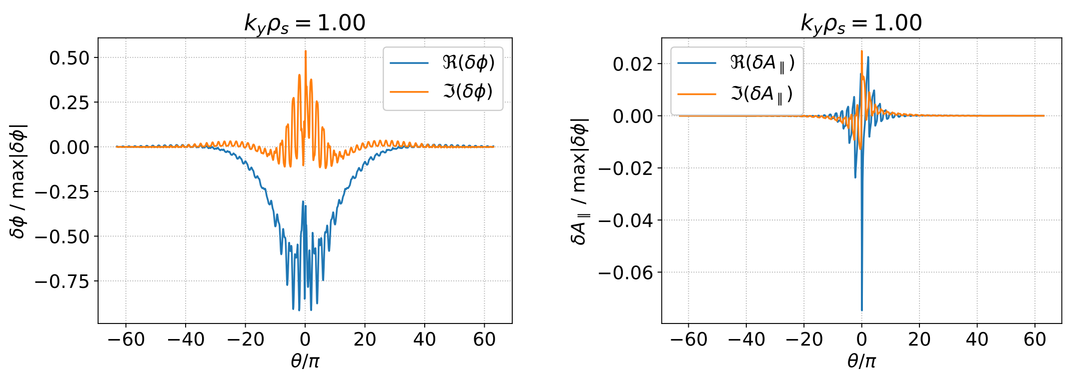

(a) **(b)**

Figure C2: *Real and imaginary part of $\delta\phi/\max|\delta\phi|$ (a) and $\delta A_\parallel/\max|\delta\phi|$ (b) as a function of θ at $k_y\rho_s = 1.0$. Results from the GS2 linear simulation at $\nu_e = 0.21\, c_s/a$.*

with $k_y\rho_s > 0.8$ from GS2 linear simulations at the reference value of electron collision frequency and at a lower value. The growth rate of the ETG instability is higher at lower ν_e than in the reference case and the ETG instability extends to modes at $k_y\rho_s \simeq 1$.

The real and imaginary parts of $\delta\phi$ and $\delta A_\parallel$ at $k_y\rho_s = 1.0$ are shown in Fig. C2. Electrostatic potential mode structure is quite extended along θ and it is similar to the one in Fig. 7, which shows $\delta\phi(\theta)$ at $k_y\rho_s = 0.5$ in the case of large electron temperature gradient values. Therefore, while the MTM instability is suppressed at large a/L_{T_e} values, the ETG instability extends into ion scale k_y region, similarly to what is observed when the value of ν_e is decreased.

These ETG modes, which are unstable at $k_y\rho_s \simeq 1$ and very extended along the magnetic field line, are similar to the ones characterised in Ref. [33]. We note that decreasing the collisionality decreases the electron detrapping frequency and therefore increases the drive at lower k_y and ω values, as shown in appendix A of Ref. [30].

References

[1] R. D. Hazeltine, D. Dobrott, and T. S. Wang. Kinetic theory of tearing instability. *The Physics of Fluids*, 18(12):1778–1786, 1975.

[2] W. Guttenfelder, J. Candy, S. M. Kaye, W. M. Nevins, E. Wang, R. E. Bell, G. W. Hammett, B. P. LeBlanc, D. R. Mikkelsen, and H. Yuh. Electromagnetic transport from microtearing mode turbulence. *Physical Review Letters*, 106(15):155004, 2011.

[3] H. Doerk, F. Jenko, M. J. Pueschel, and D. R. Hatch. Gyrokinetic microtearing turbulence. *Physical Review Letters*, 106(15):155003, 2011.

[4] D. R. Hatch, M. Kotschenreuther, S. Mahajan, P. Valanju, F. Jenko, D. Told, T. Görler, and S. Saarelma. Microtearing turbulence limiting the JET-ILW pedestal. *Nuclear Fusion*, 56(10):104003, 2016.

[5] S. Maeyama, T-H Watanabe, and A. Ishizawa. Suppression of ion-scale microtearing modes by electron-scale turbulence via cross-scale nonlinear interactions in tokamak plasmas. *Physical Review Letters*, 119(19):195002, 2017.

[6] M. J. Pueschel, D. R. Hatch, M. Kotschenreuther, A. Ishizawa, and G. Merlo. Multi-scale interactions of microtearing turbulence in the tokamak pedestal. *Nuclear Fusion*, 60(12):124005, 2020.

[7] J. F. Drake and Y. C. Lee. Kinetic theory of tearing instabilities. *The Physics of Fluids*, 20(8):1341–1353, 1977.

[8] N. T. Gladd, J. F. Drake, C. L. Chang, and C. S. Liu. Electron temperature gradient driven microtearing mode. *The Physics of Fluids*, 23(6):1182–1192, 1980.

[9] A. B. Hassam. Fluid theory of tearing instabilities. *The Physics of Fluids*, 23(12):2493–2497, 1980.

[10] P. J. Catto and M. N. Rosenbluth. Trapped electron modifications to tearing modes in the low collision frequency limit. *The Physics of Fluids*, 24(2):243–255, 1981.

[11] S. C. Cowley, R. M. Kulsrud, and T. S. Hahm. Linear stability of tearing modes. *The Physics of Fluids*, 29(10):3230–3244, 1986.

[12] J. W. Connor, S. C. Cowley, and R. J. Hastie. Micro-tearing stability in tokamaks. *Plasma Physics and Controlled Fusion*, 32(10):799, 1990.

[13] M. Hamed, M. Muraglia, Y. Camenen, X. Garbet, and O. Agullo. Impact of electric potential and magnetic drift on microtearing modes stability. *Physics of Plasmas*, 26(9):092506, 2019.

[14] D. J. Applegate, CM Roach, J. W. Connor, S. C. Cowley, W. Dorland, R. J. Hastie, and N. Joiner. Micro-tearing modes in the mega ampere spherical tokamak. *Plasma Physics and Controlled Fusion*, 49(8):1113, 2007.

[15] J. Wesson and D. J. Campbell. *Tokamaks*, volume 149. Oxford University Press, 2011.

[16] K. L. Wong, S. Kaye, D. R. Mikkelsen, J. A. Krommes, K. Hill, R. Bell, and B. LeBlanc. A quantitative account of electron energy transport in a National Spherical Tokamak Experiment plasma. *Physics of Plasmas*, 15(5):056108, 2008.

[17] W. M. Nevins, E. Wang, and J. Candy. Magnetic stochasticity in gyrokinetic simulations of plasma microturbulence. *Physical Review Letters*, 106(6):065003, 2011.

[18] A. B. Rechester and M. N. Rosenbluth. Electron Heat Transport in a Tokamak with Destroyed Magnetic Surfaces. *Physical Review Letters*, 40:38–41, 1978.

[19] C. M. Roach, D. J. Applegate, J. W. Connor, S. C. Cowley, W. D. Dorland, R. J. Hastie, N. Joiner, S. Saarelma, A. A. Schekochihin, R. J. Akers, et al. Microstability physics as illuminated in the spherical tokamak. *Plasma Physics and Controlled Fusion*, 47(12B):B323, 2005.

[20] D. Told, F. Jenko, P. Xanthopoulos, L. D. Horton, E. Wolfrum, and ASDEX Upgrade

Team. Gyrokinetic microinstabilities in ASDEX Upgrade edge plasmas. *Physics of Plasmas*, 15(10):102306, 2008.

[21] M. Valovič, R. Akers, M. De Bock, J. McCone, L. Garzotti, C. Michael, G. Naylor, A. Patel, C. M. Roach, R. Scannell, et al. Collisionality and safety factor scalings of H-mode energy transport in the MAST spherical tokamak. *Nuclear Fusion*, 51(7):073045, 2011.

[22] D. Dickinson, C. M. Roach, S. Saarelma, R. Scannell, A. Kirk, and H. R. Wilson. Microtearing modes at the top of the pedestal. *Plasma Physics and Controlled Fusion*, 55(7):074006, 2013.

[23] S. Moradi, I. Pusztai, W. Guttenfelder, T. Fülöp, and A. Mollén. Microtearing modes in spherical and conventional tokamaks. *Nuclear Fusion*, 53(6):063025, 2013.

[24] B. S. Patel, D. Dickinson, C. M. Roach, and H. Wilson. Linear gyrokinetic stability of a high β non-inductive spherical tokamak. *Nuclear Fusion*, 62(1):016009, 2021.

[25] C.J. Ajay, B. McMillan, and M. J. Pueschel. Microtearing turbulence saturation via electron temperature flattening at low-order rational surfaces. *arXiv preprint arXiv:2207.09211*, 2022.

[26] R. L. Miller, M. S. Chu, J. M. Greene, Y. R. Lin-Liu, and R. E. Waltz. Noncircular, finite aspect ratio, local equilibrium model. *Physics of Plasmas*, 5(4):973–978, 1998.

[27] Pyrokinetics. `https://github.com/pyro-kinetics/pyrokinetics`.

[28] W. Dorland, F. Jenko, M. Kotschenreuther, and B. N. Rogers. Electron temperature gradient turbulence. *Physical Review Letters*, 85(26):5579, 2000.

[29] M. Barnes, D. Dickinson, W. Dorland, P. A. Hill, C. M. Parker, J. T.and Roach, S. Biggs-Fox, N. Christen, R. Numata, et al. GS2 v8.1.2, 10.5281/zenodo.6882296, 2022.

[30] C. M. Roach, I. G. Abel, R. J. Akers, W. Arter, M. Barnes, Y. Camenen, F. J. Casson, G. Colyer, J. W. Connor, S. C. Cowley, et al. Gyrokinetic simulations of spherical tokamaks. *Plasma Physics and Controlled Fusion*, 51(12):124020, 2009.

[31] A. Zocco, N. F. Loureiro, D. Dickinson, R. Numata, and C. M. Roach. Kinetic microtearing modes and reconnecting modes in strongly magnetised slab plasmas. *Plasma Physics and Controlled Fusion*, 57(6):065008, 2015.

[32] J. Candy, E. A. Belli, and R. V. Bravenec. A high-accuracy Eulerian gyrokinetic solver for collisional plasmas. *Journal of Computational Physics*, 324:73–93, 2016.

[33] M. R. Hardman, F. I. Parra, C/ Chong, T. Adkins, M. S. Anastopoulos-Tzanis, M. Barnes, D. Dickinson, J. F. Parisi, and H. Wilson. Extended electron tails in electrostatic microinstabilities and the nonadiabatic response of passing electrons. *Plasma Physics and Controlled Fusion*, 64(5):055004, 2022.

[34] J. F. Drake, N. T. Gladd, C. S. Liu, and C. L. Chang. Microtearing modes and anomalous transport in tokamaks. *Physical Review Letters*, 44(15):994, 1980.

[35] T. Rafiq, J. Weiland, A. H. Kritz, L. Luo, and A. Y. Pankin. Microtearing modes in tokamak discharges. *Physics of Plasmas*, 23(6):062507, 2016.